Dynamics of a simplified nonlinear model offering insights into the hammering type brake squeal initiation process

Osman Taha Sen[a)] and Rajendra Singh[b)]

(Received: 19 March 2020; Revised: 10 September 2020; Accepted: 1 March 2021)

This article develops a simplified mechanical system model that offers insights into the hammering type brake squeal initiation process while overcoming a void in the literature. The proposed formulation derives a nonlinear two-degree-of-freedom model where a mass is in contact with a rigid frictional surface that moves with constant velocity. The kinematic nonlinearities arise from an arrangement of springs that support the mass, as well as from contact loss between the mass and frictional surface. First, the nonlinear governing equations are numerically solved for several normal force vector arrangements, and a wide range of dynamic responses are observed. Results show that some assumptions made in prior articles are not valid. Second, the nonlinear governing equations are linearized, and the existence of quasi-static sliding motion is sought for selected inclined spring arrangements. Third, the dynamic stability of the linearized system is examined and compared with the results of a nonlinear model. The coupled modes are found even though some contradictions between the model assumptions and linearized system solutions are observed. Finally, the nonlinear frequency responses are calculated using the multi-term harmonic balance method although only the contact loss nonlinearity is retained. Shifts in the resonant frequencies during the motion of the pad are clearly observed. In conclusion, the contact loss nonlinearity is found to be crucial, and as such, it must not be ignored for the squeal source investigation. Finally, the new model offers insight into the squeal initiation process while revealing the limitations of linearized system analyses.

Primary subject classification: 11.8.1; Secondary subject classification: 41.5

1 INTRODUCTION

There is a substantial body of literature on automotive brake noise and vibration problems, where the focus is mostly on the high frequency squeal noise as evident from two exhaustive literature reviews[1,2]. Furthermore, low-dimensional or conceptual mechanical models have been historically employed to explain plausible friction-induced noise and vibration source mechanisms in brakes. Some of these source mechanisms or squeal initiation concepts (negative damping, stick-slip, sprag-slip and mode coupling type instability) are widely discussed in the literature, and several explanations have been offered[1–8]. In addition, chaos is also suggested as a squeal mechanism by Oberst and Lai[9]. However, the hammering phenomenon[3,4] (generation of impulsive forces or motions) is yet to be adequately addressed or understood; it is the main focus of this article.

[a)] Istanbul Technical University, Department of Mechanical Engineering, Istanbul, TURKEY; email: senos@itu.edu.tr.

[b)] The Ohio State University, Department of Mechanical and Aerospace Engineering, Columbus, OH, USA; email: singh.3@osu.edu.

2 LITERATURE REVIEW

The nonlinear dynamics literature contains numerous examples of minimal order systems[10,11] although only a few relevant articles are discussed here for the sake of brevity. For instance, Hamabe et al.[12] investigated the brake squeal phenomenon with a model of dimension two. In this model, contact between the brake pad and disc was always maintained via a contact stiffness term that was assumed to be infinite. Additionally, Hamabe et al.[12] assumed two orthogonal springs, but the corresponding elastic forces were not perpendicular to the friction force vector. Hoffmann et al.[13] extended this formulation[12] with a single point contact model while retaining the two-degree-of-freedom nonlinear system approach. Unlike Hamabe et al.[12], Hoffmann et al.[13] assumed arbitrary angles between the elastic and friction force vectors. Furthermore, both studies[12,13] examined the eigenvalue problems (from the linearized system perspective), and then

the mode coupling instability was attributed to a change in the friction coefficient. Subsequently, Hoffmann and Gaul[14] developed a two-degree-of-freedom model of a mass-sliding belt system where the mass was held in position through linear elastic and dissipative elements. One of the springs was oriented at an oblique angle with respect to the friction force vector but the orientation angle was assumed to be intact irrespective of the mass motion. The system instability was investigated through the linear system, and it was found that an increase of damping can even move a stable system to an unstable regime. In another study by Kruse et al.[15], a mathematical model similar to the one developed by Hoffmann and Gaul[14] is analyzed to understand the effect of joints on the stability of a system excited with friction forces. The joint was defined as a damped harmonic oscillator that is attached to the primary mass located on the sliding belt through nonlinear elements with an oblique angle. In their study, Kruse et al.[15] assumed two different nonlinearities for the joint connection: polynomial stiffness (hardening type with cubic nonlinearity) and elasto-slip (linear spring combined with a frictional interface). The stability of this model was investigated through the eigenvalue solution of the linear system, and the limit cycle amplitudes of the nonlinear system were obtained using the harmonic balance method. Oberst and Lai[16] developed single and two-degree-of-freedom models of friction oscillators. In the single-degree-of-freedom model, they examined alternate friction laws, contact mechanisms and excitation functions and investigated the squeal behavior at different speeds of the sliding surface. It was observed that the system exhibits limit cycle behavior at the higher speeds, although the response converges to a chaotic motion at the lower speeds due to the initiation of stick-slip behavior. In their two-degree-of-freedom model, the mass was assumed to have only the planar motion (in the horizontal plane), and the velocity vector of the sliding surface was assumed to be oblique with respect to the longitudinal axis of the mass; i.e., the angle of attack for the sliding surface is nonzero. They observed that the chaotic motion dominates over a certain range of angle of attack; out of this range, the response is essentially quasi-periodic.

Charroyer et al.[17] developed a three-degree-of-freedom mathematical model of a mass-sliding belt system, where the mass was assumed as a particle located on a rigid sliding surface at constant velocity. However, mass-surface separation and sticking effects were ignored. In this particular study[17], the stability of the system was sought from the linearized equations and thus the kinematic nonlinearities (arising due to the inclined springs) were not considered. Charroyer et al.[17] investigated the effect of damping and sliding direction of the rigid surface on the system stability and observed that these parameters affect the mode coupling type instability of the system. Nevertheless, prior articles[12–17] have ignored kinematic and clearance nonlinearities. In yet another study, Charroyer et al.[18] extended their prior model[17] and introduced surface separation and sticking conditions. They proposed a new method for the identification of limit cycle behavior based on the shooting method. A good correlation between numerical time domain solutions and predicted limit cycle dynamics was observed. Overall, none of the relevant articles[12–18] has investigated the effect of inclined springs (elastic force vector arrangement) on the system stability; this is believed to be a critical issue for the brake squeal behavior. For instance, Hoffmann and Gaul[19] studied the friction-induced sprag-slip problem through a lower dimensional pin-on-disc system model which included the axial and bending motions of the pin. They determined several conditions that may trigger sprag-slip oscillations. Also, they found that the system may not have any static solution at certain values of the friction coefficient; further, no steady sliding state might exist for certain inclination angles of the pin with respect to the disc surface. Pilipchuk and Tan[20] suggested the creep-slip phenomenon as a squeal source mechanism. They examined the problem with a low-dimensional mathematical model and observed that the creep-slip action generates impulsive forces towards the end of deceleration process that could lead to squeal noise; findings of this paper[20] are then validated experimentally by Pilipchuk et al.[21]

3 SCOPE AND OBJECTIVES

The chief goal of this article is to investigate the hammering phenomenon that is proposed as a squeal source mechanism. This premise was computationally observed by Oberst et al.[22] through a finite element model of brake pad-disc system, solved using the commercial codes. They found that a partial separation between brake pad and disc contact area is possible, and this could lead to squeal initiation due to impulsive excitations on the disc by the brake pad, accompanied by an acoustic horn effect. In an experimental study by Butlin and Woodhouse[23], the effects of normal preload, sliding speed and perturbation masses on the squeal initiation on a specially designed pin-on-disc setup were investigated. Among other mechanisms, they successfully observed that the squeal is initiated at an unstable frequency and then it turns into hammering when fully developed.

This article will overcome several voids in the literature[12–14] by first proposing a new minimal order model of dimension two with kinematic, clearance (contact) and friction nonlinearities in order to show that brake disc-pad system may be excited with impulsive forces due to the contact loss. Insights into the underlying squeal phenomena will be sought via model subsets and analysis of the relevant linearized or nonlinear formulations. Accordingly, the two-degree-of-freedom model proposed for the brake squeal source investigation is displayed in Fig. 1.

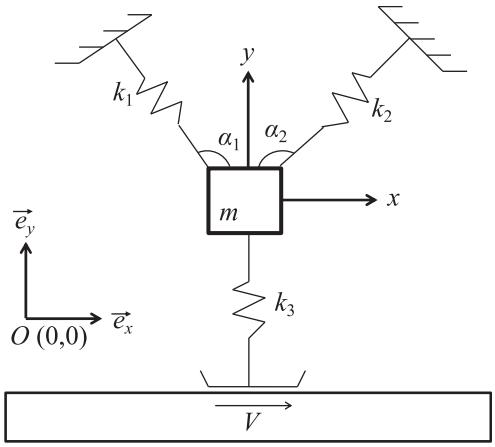

Fig. 1—Schematics of the two-degree-of-freedom mechanical system with clearance, kinematic and friction nonlinearities. Here the rigid frictional surface is translating with velocity V.

The brake pad (m) is modeled as a particle (with no geometric dimensions), and it is constrained by two linear springs (k_1 and k_2) that are positioned at arbitrary angles (α_1 and α_2). The mass is assumed to exhibit planar motion in $\vec{e}_x - \vec{e}_y$ plane, and the motions of mass m are described by two translations ($x(t)$ and $y(t)$), where $\vec{e}_x$ and $\vec{e}_y$ are the unit vectors in the x and y directions, respectively. In addition, m is positioned over a rigid surface that slides with a constant velocity V. The mass-sliding surface interface is defined via another linear contact spring (k_3) as shown in Fig. 1. Hence, the contact loss between the mass (m) and corresponding sliding surface will be investigated. A pretension (l_{pre}) is applied on k_3 that generates a constant normal force (on m) in the $\vec{e}_y$ direction; it may simulate the actuation (brake) pressure on the pad (m). Note that the mass m is defined as a rigid particle; therefore, only a single point contact (interface between the mass and the sliding surface) is assumed. Hence, only two distinct states are expected: (1) the mass and sliding surface are in contact; and (2) the surfaces are separated.

Specific objectives of this article are as follows with the Coulomb friction assumption although other nonlinear friction formulations may be utilized in the future. Table 1 summarizes the model designations (including their subsets) and their nature or utility.

1. Construct a new two-degree-of-freedom nonlinear mechanical system model with a point contact as an extension of prior models[12–14]; numerically solve the problem (model A1) for several kinematic arrangements and observe stable and unstable regimes.
2. Simplify the nonlinear model with some assumptions to obtain the linearized system (model A2) and investigate the existence of quasi-static sliding motion over a wide range of kinematic configurations; conduct a stability analysis using the linearized model (model A3), and obtain the dynamic stability maps and compare the results of the stability analysis to those from numerical method.
3. Simplify the nonlinear governing equations (model A4) by retaining the contact nonlinearities to obtain a set of piecewise linear equations and to investigate the changes in natural frequencies and apply the multi-term harmonic balance method to construct the nonlinear frequency domain response of the simplified nonlinear model.

4 DEVELOPMENT OF A NONLINEAR SQUEAL SOURCE MODEL (MODEL A1)

The nonlinear governing equations of the system of Fig. 1 are first derived. Accordingly, the position vectors of the fixed ends of three spring (with subscripts $f1$, $f2$ and $f3$) are expressed as follows where L_1, L_2 and L_3 are free lengths of the springs, and $[x_0, y_0]$ denotes the initial position of the mass:

Table 1—Subsets of the two-degree-of-freedom model of Fig. 1 and dynamic analysis features.

Model subset	Nonlinearities	Assumptions	Nature of analysis	Section of the article
A1	Friction, kinematic and clearance	—	Formulation and numerical solution	4
A2	Nonlinear equations are linearized	α_1 and α_2 are time independent. Surface separation is ignored.	Calculation of quasi-static sliding motion	5
A3	Linearized equations in the nondimensional form	α_1 and α_2 are time independent. Surface separation is ignored.	Examination of dynamic stability	6
A4	Nonlinear model with only the clearance	α_1 and α_2 are time independent. Friction nonlinearity is ignored.	Frequency response calculations	7

$$\vec{r}_{f1} = [x_0 + L_1\cos(\alpha_1)]\vec{e}_x + [y_0 + L_1\sin(\alpha_1)]\vec{e}_y \quad (1a)$$

$$\vec{r}_{f2} = [x_0 - L_2\cos(\alpha_2)]\vec{e}_x + [y_0 + L_2\sin(\alpha_2)]\vec{e}_y \quad (1b)$$

$$\vec{r}_{f3} = [x_0 + x]\vec{e}_x + [y_0 - L_3 + l_{\text{pre}}]\vec{e}_y \quad (1c)$$

Note that the fixed end of spring k_3 (Eqn. (1c)) that represents the contact interface is free to move in $\vec{e}_x$ direction, and these vectors are defined with respect to the origin (O in Fig. 1). Similarly, the position vector of m at a given instant is:

$$\vec{r} = [x_0 + x]\vec{e}_x + [y_0 + y]\vec{e}_y \quad (2)$$

Since mass m is assumed to be a particle with no geometric dimensions, the free ends of k_1, k_2 and k_3 are at the same point (node). Hence, elastic forces generated by these springs are found from the Hooke's law as expressed below:

$$F_{s,i} = -k_i\left(|\vec{r}_i - \vec{r}_{f,i}| - L_i\right)\frac{\vec{r}_i - \vec{r}_{f,i}}{|\vec{r}_i - \vec{r}_{f,i}|} \qquad i = 1,2,3 \quad (3)$$

Observe that the spring k_3 can only generate a positive (compressive) force in the $\vec{e}_y$ direction since it represents the interfacial contact. Note that m loses contact with the rigid surface when $y \geq l_{\text{pre}}$, and hence $F_{s,3} = 0$. By resolving the $\vec{e}_x$ and $\vec{e}_y$ directional elastic forces (Eqn. (3)), the following two governing equations are obtained from the force equilibria:

Observe that Eqns. (4) and (5) describe a piecewise nonlinear system due to the "sign" function that represents a loss of contact. In addition, the coefficient of friction, $\mu(V_r)$, depends on the relative velocity $V_r = \dot{x} - V$. In this formulation, the Coulomb friction model ($\mu(V_r) = \mu\ \text{sign}(V_r)$) is assumed, and therefore, the following two stick-slip cases are considered: (1) the mass sticking to the surface ($V_r = 0$), and (2) the mass moving faster ($V_r > 0$) and the mass moving slower ($V_r < 0$) than the surface. Note that in the case of sticking when $\dot{x} = V$, the dependent variable $x(t)$ is no longer an unknown, and hence, the dimension of this model would reduce to one. Furthermore, kinematic nonlinearities are apparent in the elastic force expressions of Eqns. (4) and (5).

Due to the piecewise continuous "sign" function that appears in the nonlinear governing equations, Eqns. (4) and (5) can take multiple forms. Accordingly, the numerical solutions of these equations for different cases are obtained by employing an event detection type algorithm[22]. The conditions $y - l_{\text{pre}} = 0$ and $V_r = 0$ are continuously tracked during the numerical integration, and equations are updated when either one (or both) condition is satisfied. Four geometric arrangements of the spring orientation angles α_1 and α_2 are numerically solved to explore the underlying dynamics: (a) $\alpha_1 = 0.5\pi$, $\alpha_2 = \pi$; (b) $\alpha_1 = \pi$, $\alpha_2 = 0.5\pi$; (c) $\alpha_1 = \alpha_2 = 0.75\pi$; and (d) $\alpha_1 = \alpha_2 = 0.8\overline{3}\pi$. Corresponding time histories for the normalized restoring force ($\overline{F}_{s,3}$) at the contact spring (k_3) are given in Fig. 2 along with the corresponding angular configurations. Here, the normalization is done by the total actuation force. Observe that there is a minimal difference between the first three cases, as shown in Fig. 2(a) to (c), even

$$\begin{aligned} m\ddot{x} &+ \frac{k_1\left(\sqrt{x^2 - 2xL_1\cos(\alpha_1) + y^2 - 2yL_1\sin(\alpha_1) + L_1^2} - L_1\right)}{\sqrt{x^2 - 2xL_1\cos(\alpha_1) + y^2 - 2yL_1\sin(\alpha_1) + L_1^2}}(x - L_1\cos(\alpha_1)) \\ &+ \frac{k_2\left(\sqrt{x^2 + 2xL_2\cos(\alpha_2) + y^2 - 2yL_2\sin(\alpha_2) + L_2^2} - L_2\right)}{\sqrt{x^2 + 2xL_2\cos(\alpha_2) + y^2 - 2yL_2\sin(\alpha_2) + L_2^2}}(x + L_2\cos(\alpha_2)) \\ &+ \frac{1}{2}\mu(V_r)k_3(y - l_{\text{pre}})(1 + \text{sign}(l_{\text{pre}} - y)) = 0 \end{aligned} \quad (4)$$

$$\begin{aligned} m\ddot{y} &+ \frac{k_1\left(\sqrt{x^2 - 2xL_1\cos(\alpha_1) + y^2 - 2yL_1\sin(\alpha_1) + L_1^2} - L_1\right)}{\sqrt{x^2 - 2xL_1\cos(\alpha_1) + y^2 - 2yL_1\sin(\alpha_1) + L_1^2}}(y - L_1\sin(\alpha_1)) \\ &+ \frac{k_2\left(\sqrt{x^2 + 2xL_2\cos(\alpha_2) + y^2 - 2yL_2\sin(\alpha_2) + L_2^2} - L_2\right)}{\sqrt{x^2 + 2xL_2\cos(\alpha_2) + y^2 - 2yL_2\sin(\alpha_2) + L_2^2}}(y - L_2\sin(\alpha_2)) \\ &+ \frac{1}{2}k_3(y - l_{\text{pre}})(1 + \text{sign}(l_{\text{pre}} - y)) = 0 \end{aligned} \quad (5)$$

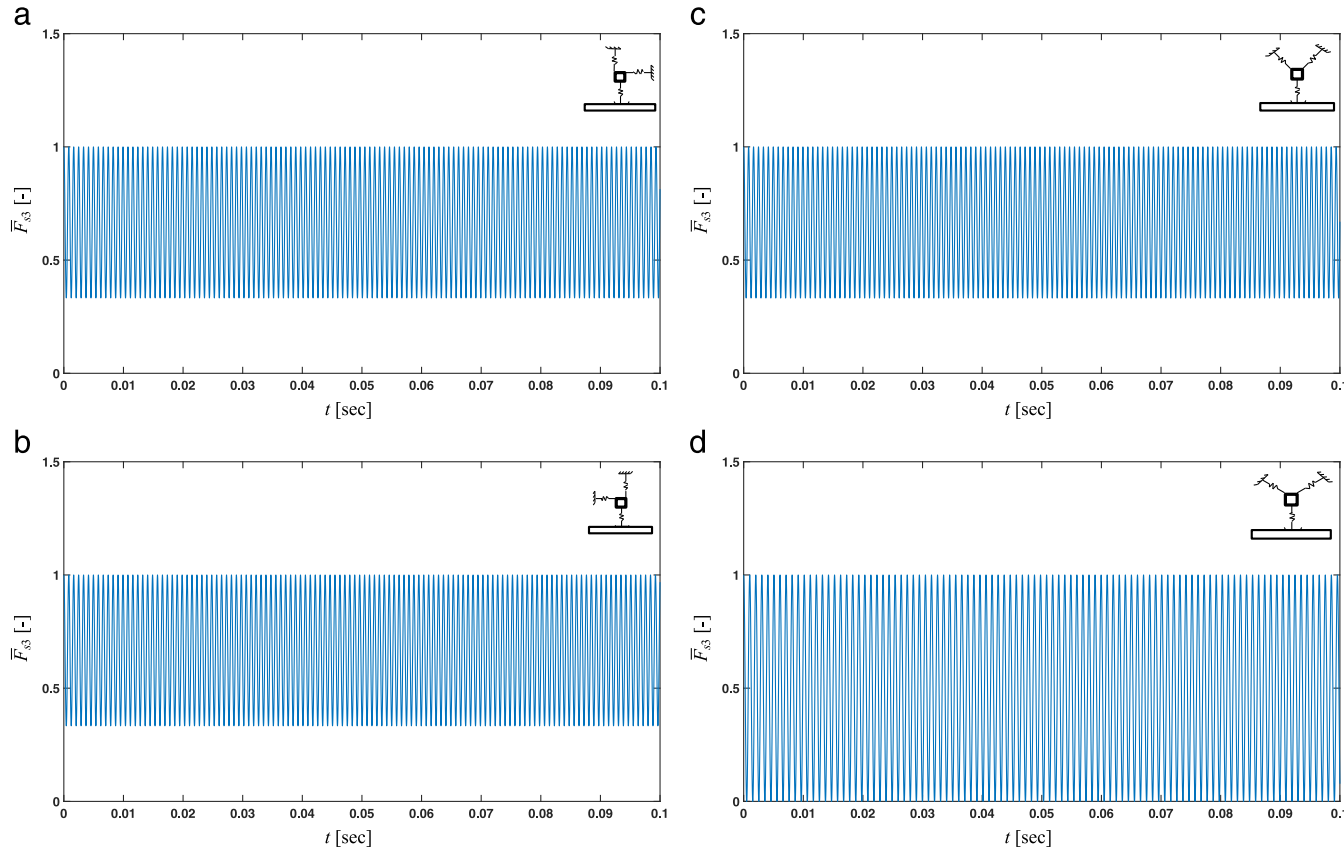

Fig. 2—Time histories of the normalized restoring force ($\overline{F}_{s3}$) at the contact spring (k_3) calculated using model A1. Here the normalization is done by the pretension applied on spring k_3 and spring configurations are shown in schematics. (a) $\alpha_1 = 0.5\pi, \alpha_2 = \pi$; (b) $\alpha_1 = \pi, \alpha_2 = 0.5\pi$; (c) $\alpha_1 = \alpha_2 = 0.75\pi$; (d) $\alpha_1 = \alpha_2 = 0.8\overline{3}\pi$.

though the angular configurations of springs k_1 and k_2 are different. Furthermore, the mass-spring contact is always maintained in these cases since $\overline{F}_{s,3} > 0$ at all times. However, the contact between the mass and its surface is lost in the last case (Fig. 2(d)) at those instants when $\overline{F}_{s,3} = 0$. Furthermore, an unstable regime is also observed for $\alpha_1 = 0.4\pi$ and $\alpha_2 = 0.6\pi$. Corresponding time histories are illustrated in Fig. 3(a) and Fig. 3(b) for x and y motions, respectively. Note that the schematics of this configuration is also embedded in the figure. The oscillatory amplitudes are unbounded, as seen in Fig. 3(a), leading to unstable dynamic responses. The limit cycle oscillations are also observed for $\alpha_1 = 0.2\pi$ and $\alpha_2 = 0.8\pi$ whose displaced system configuration in the $\vec{e}_x - \vec{e}_y$ plane is displayed in Fig. 4.

The numerical solutions are obtained for only a limited number of angular arrangements (although arbitrary). Nevertheless, quasi-static sliding motion and stability analysis are carried out for a larger interval where both α_1 and α_2 are varied from 0 to π radians as discussed in the following sections of the article. Observe that the case $\alpha_1 = \alpha_2 = \pi$ does not correspond to a negative stiffness scenario. This configuration implies that both springs (k_1 and k_2) are in the horizontal (x) direction. Evidently, the configuration $\alpha_1 = \alpha_2 = 0$ is similar to former, as both springs are again in the x direction. Theoretically, there is no difference between these two cases. However, the placement of springs for the $\alpha_1 = \alpha_2 = 0$ case would be cumbersome in practice. In order to show that these two cases represent similar dynamics, numerically obtained normalized contact forces $\overline{F}_{s,3}$ are compared in Fig. 5. Both solutions are identical, and the consecutive jumps by the mass on the sliding surface are seen due to a lack of stiffness in the vertical direction.

5 LINEARIZED SYSTEM ANALYSIS: EXISTENCE OF QUASI-STATIC SLIDING MOTION (MODEL A2)

The nonlinear governing equations (Eqns. (4) and (5)) are simplified as follows to examine the existence of quasi-static sliding motion of the system of Fig. 1. First, the piecewise continuous "sign" function in Eqns. (4) and (5) is replaced by a continuous function, $\text{sign}(z) = \tanh(\sigma z)$, where "tanh" is the hyperbolic tangent function

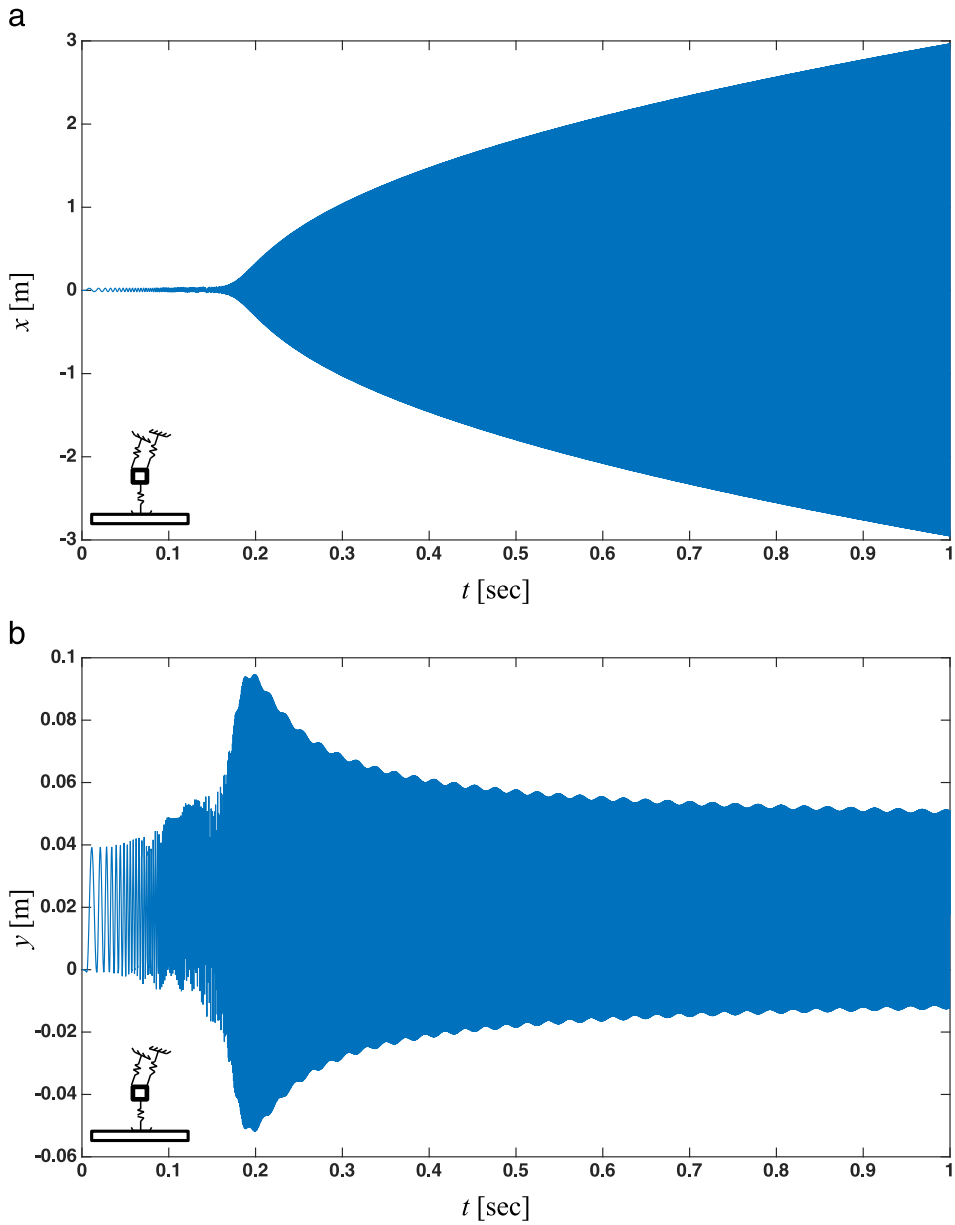

Fig. 3—Motion time histories of model A1 with $\alpha_1 = 0.4\pi$, and $\alpha_2 = 0.6\pi$. Spring configuration is shown in schematics. (a) Displacement in horizontal direction, $x(t)$; (b) Displacement in vertical direction, $y(t)$.

and σ is a regularizing factor[24–26]. Second, the Taylor series expansion is employed to linearize the governing equations about the $(x, y) = (0, 0)$ operating point to yield the following equations:

$$m\ddot{x} + K_{11}x + (K_{12} + \mu K_3)y = 0.5\mu k_3 l_{\text{pre}}\left(\tanh\left(\sigma l_{\text{pre}}\right) + 1\right) \tag{6}$$

$$m\ddot{y} + K_{12}x + (K_{22} + K_3)y = 0.5 k_3 l_{\text{pre}}\left(\tanh\left(\sigma l_{\text{pre}}\right) + 1\right) \tag{7}$$

where the linearized stiffness terms are defined as:

$$K_{11} = k_1 \cos^2(\alpha_1) + k_2 \cos^2(\alpha_2) \tag{8a}$$

$$K_{22} = k_1 \sin^2(\alpha_1) + k_2 \sin^2(\alpha_2) \tag{8b}$$

$$K_{12} = k_1 \cos(\alpha_1)\sin(\alpha_1) - k_2 \cos(\alpha_2)\sin(\alpha_2) \tag{8c}$$

$$K_3 = 0.5 k_3 \left(\tanh\left(\sigma l_{\text{pre}}\right) + \sigma l_{\text{pre}} - \sigma l_{\text{pre}} \tanh^2\left(\sigma l_{\text{pre}}\right) + 1\right) \tag{8d}$$

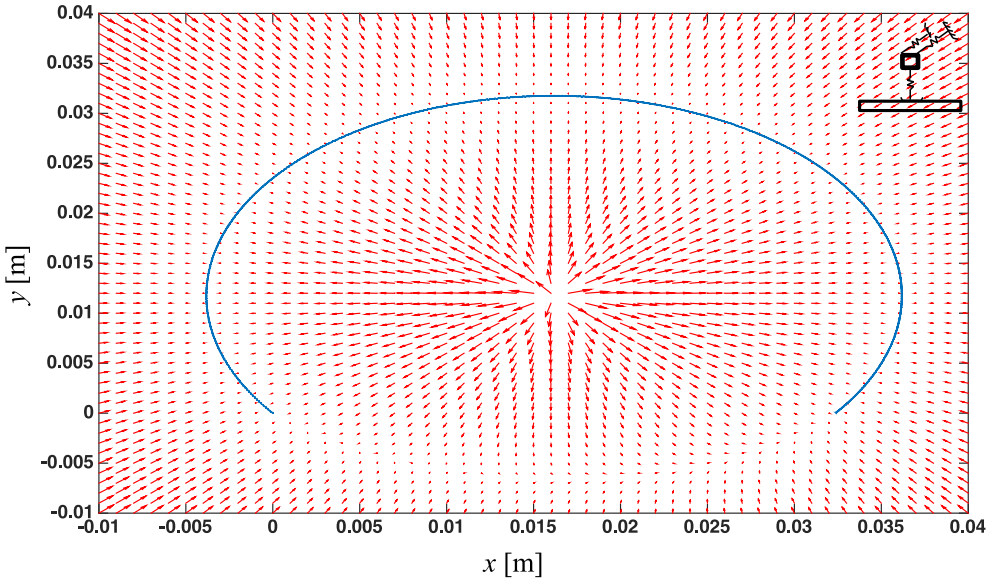

Fig. 4—Displaced system configuration and limit cycle behavior of model A1 with $\alpha_1 = 0.2\pi$ and $\alpha_2 = 0.8\pi$. Spring configuration is shown in schematics.

Observe that Eqns. (6) and (7) are linear, and the mass-surface separation effect is no longer considered. Even though the hyperbolic tangent function emerges from the signum function that defines the surface separation effect, the truncated Taylor series expansion mathematically eliminates the possibility of any surface separation.

To find the $\alpha_1 - \alpha_2$ values where quasi-static sliding motion is possible, Eqns. (6) and (7) are written in matrix form as:

$$\begin{bmatrix} m & 0 \\ 0 & m \end{bmatrix} \begin{Bmatrix} \ddot{x} \\ \ddot{y} \end{Bmatrix} + \begin{bmatrix} K_{11} & K_{12} \\ K_{12} & K_{22} \end{bmatrix} \begin{Bmatrix} x \\ y \end{Bmatrix} = \begin{Bmatrix} \mu R_n \\ -F_n + R_n \end{Bmatrix}. \tag{9}$$

Here the pretension l_{pre} is applied on the spring k_3 in Eqns. (6) and (7) although it is now defined as an external force F_n acting on the mass m in Eqn. (9). Furthermore, the

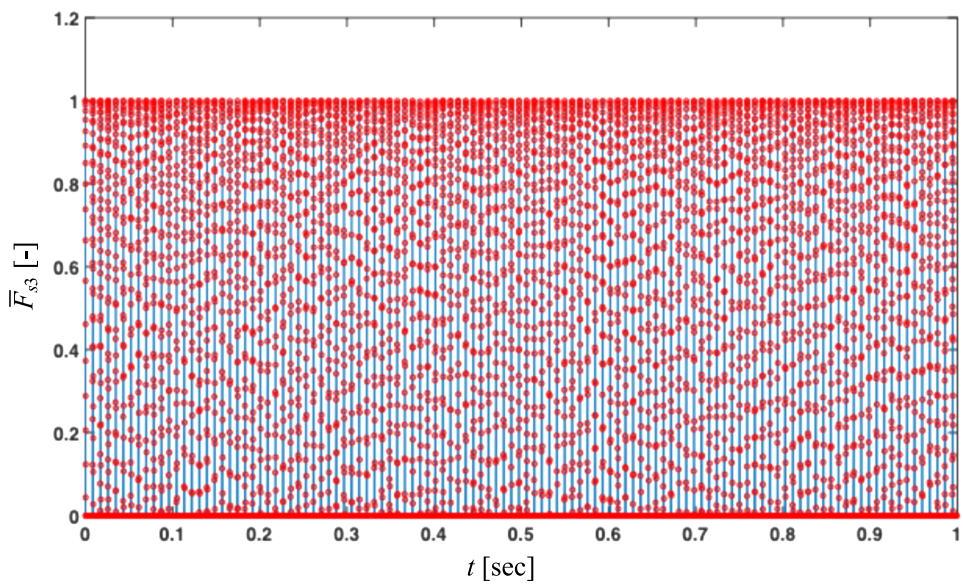

Fig. 5—Time histories of the normalized restoring forces ($\overline{F}_{s3}$) at the contact spring (k_3) calculated using model A1. Key: ——, $\alpha_1 = \alpha_2 = \pi$; ○, $\alpha_1 = \alpha_2 = 0$.

reaction force at the contact interface is given by R_n. For quasi-static motion, m must not have any acceleration, i.e., $\ddot{x} = 0$ and $\ddot{y} = 0$. Hence, Eqn. (9) becomes:

$$\begin{bmatrix} K_{11} & K_{12} \\ K_{12} & K_{22} \end{bmatrix} \begin{Bmatrix} x \\ y \end{Bmatrix} = \begin{Bmatrix} \mu R_n \\ -F_n + R_n \end{Bmatrix} \tag{10}$$

For quasi-static sliding motion, m should be always in contact with the sliding surface, and thus, the motion in vertical direction should be zero ($y = 0$). This leads to the following condition for the existence of the quasi-static sliding motion as derived from Eqn. (10):

$$\mu < \frac{k_1 \cos^2(\alpha_1) + k_2 \cos^2(\alpha_2)}{k_1 \cos(\alpha_1)\sin(\alpha_1) - k_2 \cos(\alpha_2)\sin(\alpha_2)}. \tag{11}$$

This condition is checked over the $0 \le \alpha_1 \le \pi$ and $0 \le \alpha_2 \le \pi$ region and corresponding mapping is depicted in Fig. 6 along with stability analysis. Note that the quasi-static sliding motion is only possible within the white colored regions of Fig. 6.

6 STABILITY ANALYSIS USING THE LINEARIZED MODEL (MODEL A3)

The dynamic stability of the system is sought with the linearized equations (Eqns. (6) and (7)) although they are first normalized by defining the following nondimensional parameters.

$$\omega_{11} = \sqrt{\frac{K_{11}}{m}}, \quad \omega_{12} = \sqrt{\frac{K_{12}}{m}}, \quad \omega_{22} = \sqrt{\frac{K_{22}}{m}}, \quad \omega_3 = \sqrt{\frac{K_3}{m}}, X = \frac{x}{l_{\text{pre}}}, \quad Y = \frac{y}{l_{\text{pre}}}, \quad \tau = \omega_{11} t \tag{12a – g}$$

Equations (6) and (7) are converted into nondimensional form as follows:

$$X'' + X + \left(\frac{\omega_{12}^2 + \mu\omega_3^2}{\omega_{11}^2}\right) Y = 0.5\mu \frac{k_3}{K_{11}} \left(\tanh\left(\sigma l_{\text{pre}}\right) + 1\right) \tag{13}$$

$$Y'' + \frac{\omega_{12}^2}{\omega_{11}^2} X + \left(\frac{\omega_{22}^2 + \omega_3^2}{\omega_{11}^2}\right) Y = 0.5 \frac{k_3}{K_{11}} \left(\tanh\left(\sigma l_{\text{pre}}\right) + 1\right) \tag{14}$$

where $()' = \mathrm{d}()/\mathrm{d}\tau$. To assess the dynamic stability of the given system, the Jacobian matrix is calculated around the static equilibrium (X^*, Y^*) where:

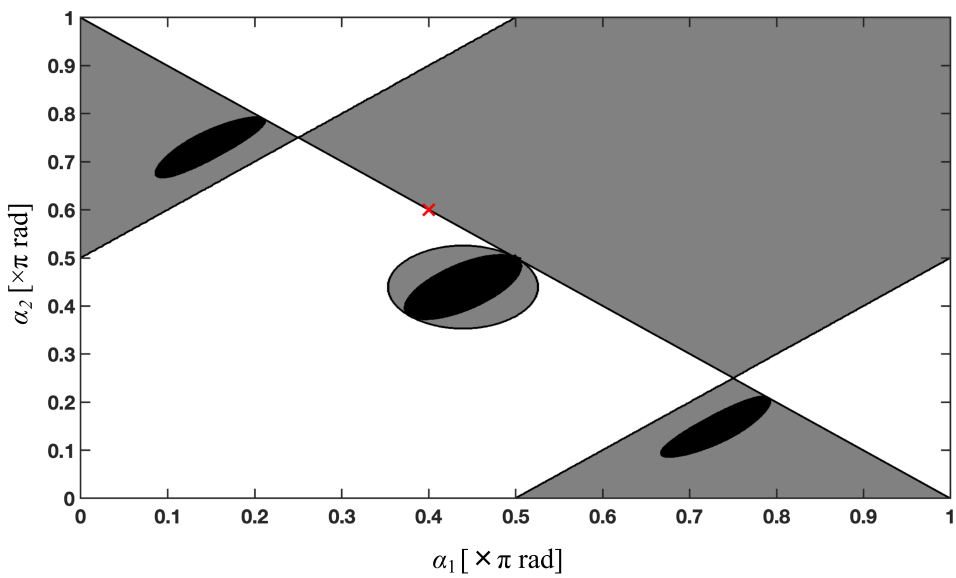

Fig. 6—Quasi-static sliding motion (model A2) and stability regions (model A3) of the linearized system over $0 \le \alpha_1 \le \pi$ and $0 \le \alpha_2 \le \pi$. Color code: (1) white, region where quasi-static sliding is possible; (2) gray, region where quasi-static sliding is not possible; (3) black, region where unstable regime is observed. As seen, all unstable regions (black regions) locate where quasi-static sliding is not possible (gray regions). The unstable case of Fig. 3 is depicted with "×."

$$X^* = 0.5\left(\frac{k_3}{K_{11}}\right)\frac{\omega_{11}^2\left(\omega_{12}^2 - \mu\omega_{22}^2\right)}{\omega_{12}^4 + \mu\omega_{12}^2\omega_3^2 - \omega_{11}^2\omega_{22}^2 - \omega_{11}^2\omega_3^2}\left(\tanh\left(\sigma l_{\text{pre}}\right) + 1\right) \tag{15a}$$

$$Y^* = 0.5\left(\frac{k_3}{K_{11}}\right)\frac{\omega_{11}^2\left(\mu\omega_{12}^2 - \omega_{11}^2\right)}{\omega_{12}^4 + \mu\omega_{12}^2\omega_3^2 - \omega_{11}^2\omega_{22}^2 - \omega_{11}^2\omega_3^2}\left(\tanh\left(\sigma l_{\text{pre}}\right) + 1\right) \tag{15b}$$

By transforming the dependent variables to $\left(\overline{X}, \overline{Y}\right) = \left(X + X^*, Y + Y^*\right)$ that define their static equilibria, the nondimensional governing equations (Eqns. (13) and (14)) are rewritten as:

$$\bar{X}'' + \bar{X} + \left(\frac{\omega_{12}^2 + \mu\omega_3^2}{\omega_{11}^2}\right)\bar{Y} = 0 \tag{16}$$

$$\bar{Y}'' + \frac{\omega_{12}^2}{\omega_{11}^2}\bar{X} + \left(\frac{\omega_{22}^2 + \omega_3^2}{\omega_{11}^2}\right)\bar{Y} = 0. \tag{17}$$

Based on Eqns. (16) and (17), a complex eigenvalue solution of the Jacobian matrix is utilized to assess the dynamic stability. This solution is performed for many values of α_1 and α_2 where α_1 and α_2 are varied over the closed intervals of $[0, \pi]$. The stability maps from the linearized system analysis are displayed in Fig. 6, where the following color codes are employed: (1) quasi-static sliding is possible in the white colored regions; (2) quasi-static sliding is not possible in the gray colored regions; and (3) unstable regime is observed in the black colored regions. Observe that quasi-static sliding motion is not possible in any of the unstable regions, and the system is always stable as long as the quasi-static sliding motion persists. Furthermore, the unstable case for $\alpha_1 = 0.4\pi$ and $\alpha_2 = 0.6\pi$ (see Fig. 3 for the corresponding time histories) is in fact a stable response based on the stability map of Fig. 6 (shown with a red $\times$ point in Fig. 6). Hence, the stability analysis based on the linear system premise alone cannot accurately predict the dynamics. This discrepancy is due to the linearization process (such as the Taylor series expansion) since the nonlinear terms in Eqns. (4) and (5) get converted into first-order polynomials. Thus, the piecewise continuous terms drop out, and the linear system (Eqns. (6) and (7)) ends up describing the behavior that predicts contact under all conditions. This implies that the spring k_3 works simultaneously in both compression and tension which is not physically possible. Note that the spring k_3 represents the contact in between the mass and the sliding surface and thus can only operate in compression. When a tension is applied to this spring, contact will be lost, and thus, the spring k_3 cannot be active.

The regions where the prior stability analysis (with the nonlinear formulation) is valid are shown in Fig. 7. This map is obtained by checking the existence of quasi-static sliding motion by using the numerical solutions of nonlinear governing equations. Hence, Eqns. (4) and (5) are numerically solved over a broader time interval, and the occurrence of surface separation is sought over the time span of integration. When the surface separation is not observed, the stability analysis is assumed to be valid (as indicated by the gray and black colored regions). Consequently, the linear stability analysis can be used to predict the stability of the system only in this region. Gray-colored region is where the system is found to be stable via the linearized analysis, and the black-colored region is where the system stability cannot be preserved. In contrast, the stability analysis is assumed to be invalid for the configurations $[\alpha_1, \alpha_2]$ when the surface separation is detected (as indicated by the white colored regions in Fig. 7). Overall, the linearized system analysis cannot be used to determine the stability of this system.

Similar claims were made by Hochlenert[27] who observed that the stability boundary of a linearized 12-degree-of-freedom disc brake system was not satisfactory since the stability becomes insensitive to angular speed at higher friction coefficient values and vice versa. Therefore, Hochlenert[27] carried out a nonlinear stability analysis to obtain more accurate results. In a related study, Sinou[28] examined the stability of a linearized system, although the time domain solutions obtained via a nonlinear finite element model revealed the interesting dynamics in the frequency domain (through the wavelet transform). Furthermore, Soobbarayen et al.[29] developed a nonlinear finite element model of the disc brake system where friction and contact loss nonlinearities were both considered. Soobbarayen et al.[29] first solved the complex eigenvalue problem of a system that was linearized about the steady sliding equilibrium point and obtained the unstable frequencies. They observed that the stability analysis may lead to under/overestimation of the unstable modes due to the violation of the linear system conditions during the nonlinear simulations (in time domain). It was found that a stable configuration (as predicted by the linear system stability analysis) could lead to an unstable response by a fast ramp load applied on the pads. Likewise, Zhang et al.[30] concluded that the linear system solution approaches could lead to misinterpretations, and thus, a nonlinear stability analysis was recommended. Interestingly, Zhang et al.[30] claimed that the discrepancies between linear and nonlinear analyses become more pronounced for a strongly nonlinear problem. Indeed, that is what has observed for the nonlinear mechanical system of this article. In another work, Oberst and Lai[31] developed two computational models (pad-on-plate and pad-on-disc) to better understand the effects of material properties. They observed that complex eigenvalue analysis may fail to detect the unstable vibration modes, while in-plane pad modes are found to be a major cause for squeal noise based on the

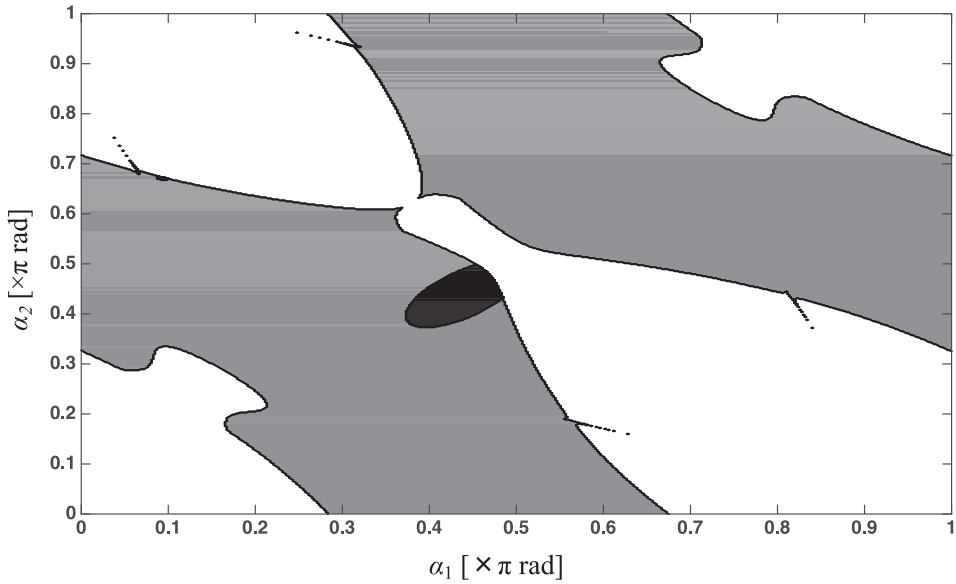

Fig. 7—Validity of the dynamic stability map (of Fig. 6) over $0 \le \alpha_1 \le \pi$ and $0 \le \alpha_2 \le \pi$. Color code: (1) white, regions where the linear system analysis (model A3) is invalid; (2) gray, regions where the system exhibits stable dynamics; (3) black, regions where the system exhibits unstable dynamics. Note that the stable and unstable regimes are determined from the nonlinear system analysis (model A1).

kinetic and dissipated energy spectra. Based on the time domain analysis of a nonlinear model, Oberst and Lai[32] observed that the dissipated energy might be even negative at those frequencies that were found to be stable with the complex eigenvalue analysis. Furthermore, the out-of-plane modes of the pad are also found to be important for squeal initiation[32].

7 FREQUENCY RESPONSES OF THE NONLINEAR MODEL CONSIDERING ONLY THE CONTACT LOSS (MODEL A4)

To understand the frequency characteristics of the two-degree-of-freedom model, the nonlinear governing equations (Eqns. (4) and (5)) are first simplified in the following manner: (a) the friction nonlinearity is ignored by assuming $V_r < 0$ at all times; (b) the friction coefficient μ is assumed to be constant; and (c) kinematic nonlinearities due to the orientation angles α_1 and α_2 are eliminated with the Taylor series expansion. Only the contact loss nonlinearity is retained and the piecewise nonlinear equations are obtained as:

$$m\ddot{x} + K_{11}x + K_{12}y + 0.5\mu k_3\left(y - l_{\text{pre}}\right)\left(1 + \text{sign}\left(l_{\text{pre}} - y\right)\right) = 0 \tag{18}$$

$$m\ddot{y} + K_{12}x + K_{22}y + 0.5k_3\left(y - l_{\text{pre}}\right)\left(1 + \text{sign}\left(l_{\text{pre}} - y\right)\right) = 0 \tag{19}$$

Observe that Eqns. (18) and (19) can be written in terms of two different sets of the linear equations based on the sign of the term $(y - l_{\text{pre}})$. Consider the case $y - l_{\text{pre}} < 0$ that represents sliding motion with contact. Hence, Eqns. (18) and (19) become a set of coupled nonhomogeneous linear ordinary differential equations.

$$m\ddot{x} + K_{11}x + (K_{12} + \mu k_3)y = \mu k_3 l_{\text{pre}} \tag{20}$$

$$m\ddot{y} + K_{12}x + (K_{22} + k_3)y = k_3 l_{\text{pre}} \tag{21}$$

Corresponding natural frequency expressions (for modes 1 and 2) are derived as follows through the eigenvalue problem solution of Eqns. (20) and (21):

$$\omega_1 = \sqrt{\frac{K_{11} + K_{22} + k_3 - \sqrt{\begin{matrix}K_{11}^2 - 2K_{11}K_{22} + K_{22}^2 + 4K_{12}^2 \\ -2K_{11}k_3 + 4\mu K_{12}k_3 + 2K_{22}k_3 + k_3^2\end{matrix}}}{2m}} \tag{22a}$$

$$\omega_2 = \sqrt{\frac{K_{11} + K_{22} + k_3 + \sqrt{\begin{matrix}K_{11}^2 - 2K_{11}K_{22} + K_{22}^2 + 4K_{12}^2 \\ -2K_{11}k_3 + 4\mu K_{12}k_3 + 2K_{22}k_3 + k_3^2\end{matrix}}}{2m}}. \tag{22b}$$

Next, examine the surface separation case when the condition is $y - l_{\text{pre}} \ge 0$. Now a set of coupled homogeneous linear differential equations emerges.

$$m\ddot{x} + K_{11}x + K_{12}y = 0 \tag{23}$$

$$m\ddot{y} + K_{12}x + K_{22}y = 0 \tag{24}$$

Their natural frequency expressions are found as:

$$\omega_1 = \sqrt{\frac{K_{11} + K_{22} - \sqrt{K_{11}^2 - 2K_{11}K_{22} + K_{22}^2 + 4K_{12}^2}}{2m}} \tag{25a}$$

$$\omega_2 = \sqrt{\frac{K_{11} + K_{22} + \sqrt{K_{11}^2 - 2K_{11}K_{22} + K_{22}^2 + 4K_{12}^2}}{2m}}. \tag{25b}$$

Based on the natural frequency expressions, changes in ω_1 and ω_2 with respect to α_1 and α_2 over the closed intervals $[0, \pi]$ are mapped in Figs. 8 and 9. First, it is seen from Fig. 8(a) that $\omega_1 = 0$ at the vicinity of $\alpha_1 = \alpha_2 = \pi/2$ for the contact case. However, for the surface separation case (Fig. 8(b)), $\omega_1 = 0$ is valid in the neighborhood of $\alpha_1 + \alpha_2 = n\pi$ where n is an integer including zero. Furthermore, ω_1 tends to be maximum when $\alpha_1 + \alpha_2 = 0.5n\pi$. The conditions that lead to $\omega_1 = 0$ are also valid for ω_2 to be maximum as seen in Fig. 9. In other words, two natural frequencies of the system tend to shift in the opposite directions; i.e., while ω_1 increases, ω_2 decreases and vice versa.

The nonlinear frequency responses of the simplified system, described by Eqns. (18) and (19), are obtained by implementing the multi-term harmonic balance method. First, the discontinuous signum functions in Eqns. (18) and (19) are replaced by analytic hyperbolic tangent functions, i.e., $\mathrm{sign}(l_{\mathrm{pre}} - y) = \tanh(\sigma(l_{\mathrm{pre}} - y))$; here, the regularizing factor σ should be a relatively large number for a better approximation of the original function. Furthermore, the equations are transformed from time domain (t) to the spatial domain (θ) by assuming $\theta = \omega t$, and the corresponding derivatives are defined with respect to θ as $\mathrm{d}()/\mathrm{d}t = \omega \mathrm{d}()/\mathrm{d}\theta$.

$$\begin{aligned}&\omega^2 m x'' + K_{11}x + K_{12}y \\ &\quad + 0.5\mu k_3 (y - l_{\mathrm{pre}})(1 + \tanh(\sigma(l_{\mathrm{pre}} - y))) \\ &\quad = 0\end{aligned} \tag{26}$$

$$\begin{aligned}&\omega^2 m y'' + K_{12}x + K_{22}y \\ &\quad + 0.5k_3 (y - l_{\mathrm{pre}})(1 + \tanh(\sigma(l_{\mathrm{pre}} - y))) \\ &\quad = 0\end{aligned} \tag{27}$$

where $()' = \mathrm{d}()/\mathrm{d}\theta$. Furthermore, the steady state solutions of Eqns. (26) and (27) are assumed to be in the forms of truncated Fourier series as:

$$x(\theta) = a_0 + \sum_{n=1}^{N_h} a_{2n-1}\sin(n\theta) + a_{2n}\cos(n\theta) \tag{28a}$$

$$y(\theta) = b_0 + \sum_{n=1}^{N_h} b_{2n-1}\sin(n\theta) + b_{2n}\cos(n\theta) \tag{28b}$$

where N_h is the number of harmonics retained in Fourier series expansions. Note that the sub-harmonics are not included in the above expansion. Solution assumptions given with Eqns. (28a) and (28b) are discretized as $x = \mathbf{\Gamma a}$ and $y = \mathbf{\Gamma b}$, where $\mathbf{a}$ and $\mathbf{b}$ are Fourier coefficient vectors and $\mathbf{\Gamma}$ is the discrete Fourier transform matrix defined as:

$$\mathbf{\Gamma} = \begin{bmatrix} 1 & \sin(\theta_0) & \cos(\theta_0) & \cdots & \sin(N_h\theta_0) & \cos(N_h\theta_0) \\ 1 & \sin(\theta_1) & \cos(\theta_1) & \cdots & \sin(N_h\theta_1) & \cos(N_h\theta_1) \\ \vdots & \vdots & \vdots & \ddots & \vdots & \vdots \\ 1 & \sin(\theta_{N-1}) & \cos(\theta_{N-1}) & \cdots & \sin(N_h\theta_{N-1}) & \cos(N_h\theta_{N-1}) \end{bmatrix} \tag{29}$$

where N is the number of points used in discretization, and $N \geq 2N_h$ must be satisfied in order to prevent aliasing. The derivatives in Eqns. (26) and (27) are defined in discrete form as $x'' = \mathbf{\Gamma D^2 a}$ and $y'' = \mathbf{\Gamma D^2 b}$, where $\mathbf{D}$ is the differential operator matrix that is defined as:

$$\mathbf{D} = \begin{bmatrix} 0 & 0 & 0 & \cdots & 0 & 0 \\ 0 & 0 & -1 & \cdots & 0 & 0 \\ 0 & 1 & 0 & \cdots & 0 & 0 \\ \vdots & \vdots & \vdots & \ddots & \vdots & \vdots \\ 0 & 0 & 0 & \cdots & 0 & -N_h \\ 0 & 0 & 0 & \cdots & N_h & 0 \end{bmatrix} \tag{30}$$

For the discretization of the nonlinear terms in Eqns. (26) and (27), the discontinuous functions are defined as $\mathbf{h} = \tanh(\sigma(l_{\mathrm{pre}} - \mathbf{\Gamma b}))$ and $\mathbf{g} = y\tanh(\sigma(l_{\mathrm{pre}} - \mathbf{\Gamma b}))$. These nonlinear functions are also expanded in truncated Fourier series and then discretized as $\mathbf{h} = \mathbf{\Gamma c}$ and $\mathbf{g} = \mathbf{\Gamma d}$, where $\mathbf{c}$ and $\mathbf{d}$ are also unknown Fourier coefficient vectors. Equations (26) and (27) are now written in discrete form as:

$$\begin{aligned}&\omega^2 m\mathbf{\Gamma D^2 a} + K_{11}\mathbf{\Gamma a} + K_{12}\mathbf{\Gamma b} \\ &\quad + 0.5\mu k_3 \mathbf{\Gamma}(\mathbf{b} + \mathbf{d} - l_{\mathrm{pre}}\mathbf{c}) \\ &\quad = 0.5\mu k_3 l_{\mathrm{pre}}\end{aligned} \tag{31}$$

$$\begin{aligned}&\omega^2 m\mathbf{\Gamma D^2 b} + K_{12}\mathbf{\Gamma a} + K_{22}\mathbf{\Gamma b} \\ &\quad + 0.5k_3 \mathbf{\Gamma}(\mathbf{b} + \mathbf{d} - l_{\mathrm{pre}}\mathbf{c}) \\ &\quad = 0.5k_3 l_{\mathrm{pre}}.\end{aligned} \tag{32}$$

Note that Eqns. (31) and (32) form a set of coupled nonlinear algebraic equations, and $\mathbf{\Gamma}$ can be dropped by premultiplying the equations with the pseudo-inverse of $\mathbf{\Gamma}$,

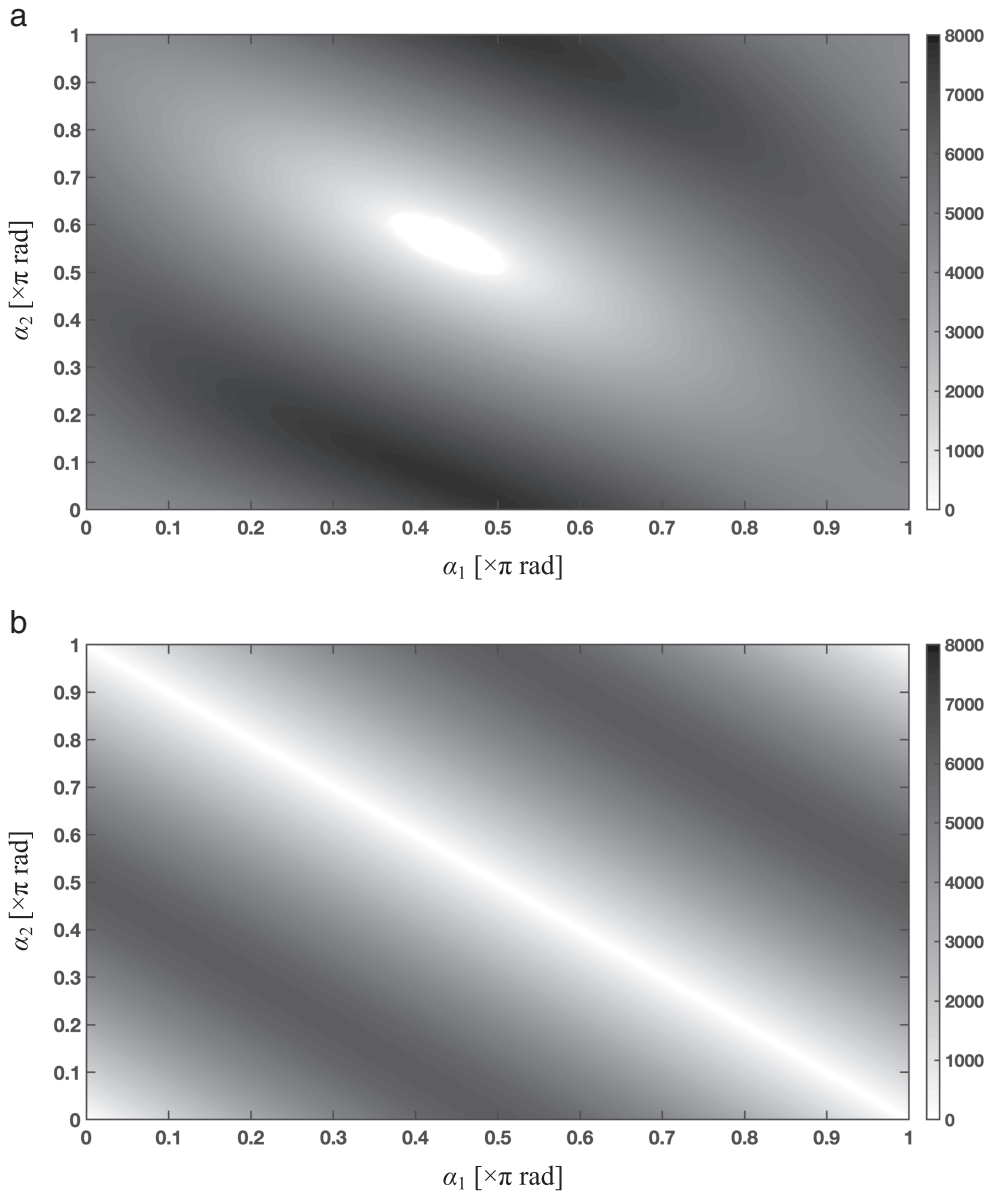

Fig. 8—First natural frequency (in rad/s unit) of the system of model A4 with respect to α_1 and α_2. (a) Contact case (Eqn. (22a)); (b) Surface separation case (Eqn. (25a)).

which is defined as $\mathbf{\Gamma}^{+} = \left(\mathbf{\Gamma}^{\mathrm{T}}\mathbf{\Gamma}\right)^{-1}\mathbf{\Gamma}^{\mathrm{T}}$. The unknown vectors $\mathbf{a}$ and $\mathbf{b}$ that are related to the dependent variables in Eqns. (31) and (32) are found by using the Newton-Raphson method, where the idea is to minimize the residues based on the assumed solutions given with Eqns. (28a) and (28b). The residue functions from Eqns. (31) and (32) are derived as:

$$\mathbf{R}_1 = \omega^2 m\mathbf{D}^2\mathbf{a} + K_{11}\mathbf{a} + K_{12}\mathbf{b} + 0.5\mu k_3\left(\mathbf{b} + \mathbf{\Gamma}^{+}\mathbf{g} - l_{\mathrm{pre}}\mathbf{\Gamma}^{+}\mathbf{h}\right) - \mathbf{Q}_1 \tag{33}$$

$$\mathbf{R}_2 = \omega^2 m\mathbf{D}^2\mathbf{b} + K_{11}\mathbf{a} + K_{12}\mathbf{b} + 0.5k_3\left(\mathbf{b} + \mathbf{\Gamma} + \mathbf{g} - l_{\mathrm{pre}}\mathbf{\Gamma} + \mathbf{h}\right) - \mathbf{Q}_2 \tag{34}$$

where $\mathbf{Q}_1$ and $\mathbf{Q}_2$ are the vectors formed from the nonhomogeneous terms. Finally, the Newton-Raphson method is applied as:

$$\boldsymbol{\eta}_{i+1} = \boldsymbol{\eta}_i - \mathbf{J}_i^{-1}\mathbf{R}_i \tag{35}$$

where $\boldsymbol{\eta} = [\mathbf{a}\ \ \mathbf{b}\ \ \omega]^{\mathrm{T}}$, $\mathbf{R} = [\mathbf{R_1}\ \ \ \mathbf{R_2}]^{\mathrm{T}}$, and $\mathbf{J}$ is the Jacobian matrix as defined below:

$$\mathbf{J} = \begin{bmatrix} \dfrac{\partial \mathbf{R_1}}{\partial \mathbf{a}} & \dfrac{\partial \mathbf{R_1}}{\partial \mathbf{b}} & \dfrac{\partial \mathbf{R_1}}{\partial \omega} \\ \dfrac{\partial \mathbf{R_2}}{\partial \mathbf{a}} & \dfrac{\partial \mathbf{R_2}}{\partial \mathbf{b}} & \dfrac{\partial \mathbf{R_2}}{\partial \omega} \end{bmatrix}. \tag{36}$$

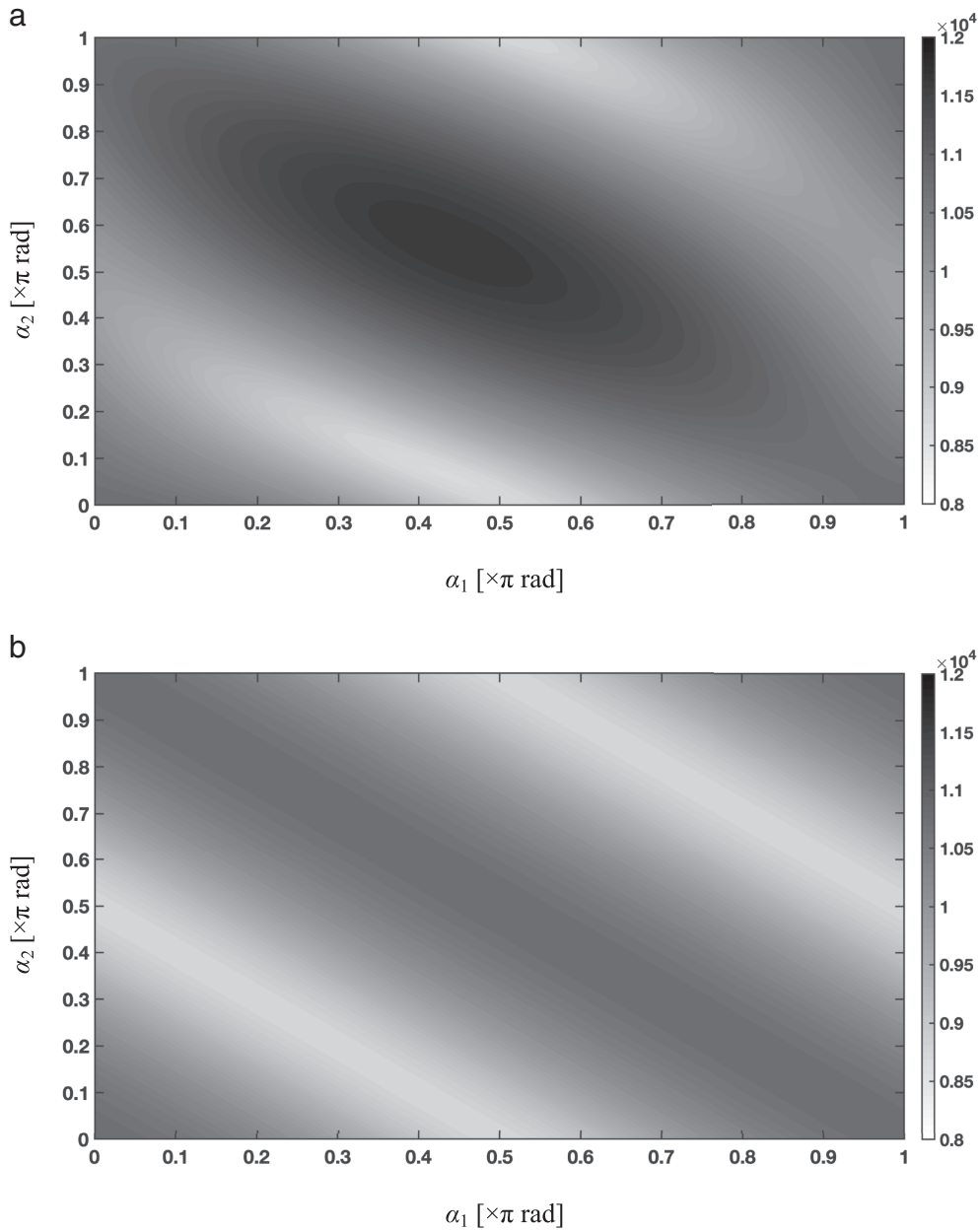

Fig. 9—Second natural frequency (in rad/s unit) of the system of model A4 with respect to α_1 and α_2. (a) Contact case (Eqn. (22b)); (b) Surface separation case (Eqn. (25b)).

Equation (35) is iteratively solved, and the $x(t)$ and $y(t)$ response amplitudes in the vicinity of ω_1 and ω_2 are shown in Figs. 10 to 13 for different values of α_1 and α_2. Observe that inhe first three cases ($[\alpha_1, \alpha_2] = [\pi/2, \pi]$,$[\alpha_1, \alpha_2] = [\pi, \pi/2]$ and $[\alpha_1, \alpha_2] = [3\pi/4, 3\pi/4]$), nonlinear frequency response amplitudes do not show a significant difference with each other as also observed in the time domain solutions (Fig. 2(a–c)). Moreover, only a single peak in the vicinity of ω_1 is seen that corresponds to a motion in the x direction (Figs. 10(a), 11(a) and 12(a)). In other words, m moves only in the x direction around ω_1 without any participation from the motion in y direction. However, there are resonant peaks in both x and y direction responses around ω_2 (Figs. 10(b), 11(b) and 12(b)). Responses in the y direction pass the $y = l_{\text{pre}}$ threshold (shown with a solid line), and the frequency peaks bend towards smaller frequencies since $k_3 = 0$ when $y > l_{pre}$. This is due to a decrease in the effective system stiffness. For the last case ($[\alpha_1, \alpha_2] = [5\pi/6, 5\pi/6]$), it is seen from Fig. 13 that the first and second modes of the system are switched. The isolated mode moves to the second mode, and the contact loss now occurs at the first mode.

8 PRIOR EXPERIMENTS AND NOISE CONTROL IMPLICATIONS

The findings of this article are qualitatively supported by prior limited measurements as reported in the literature.

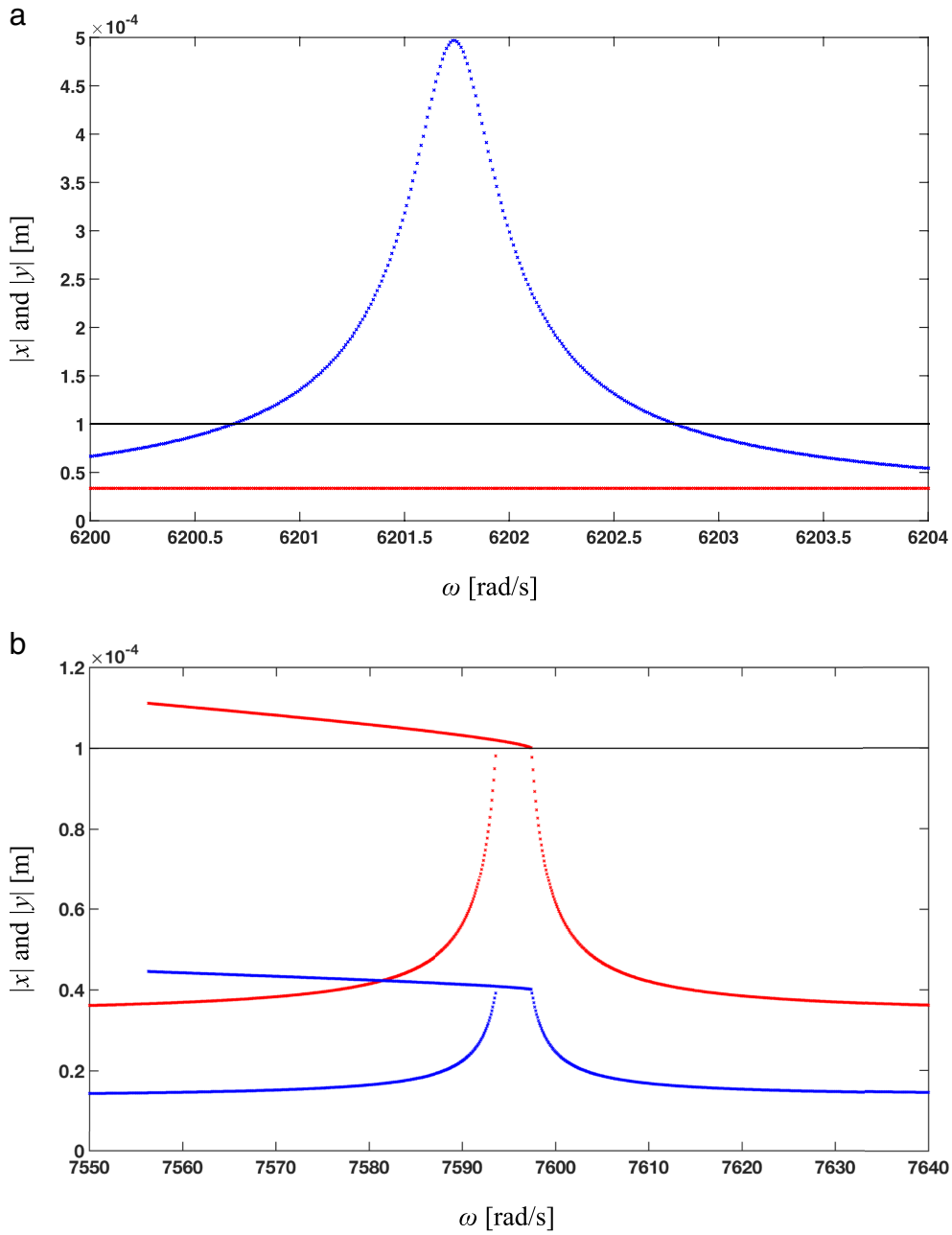

Fig. 10—Nonlinear frequency response of the simplified model (model A4) for $\alpha_1 = \pi/2$, $\alpha_2 = \pi$. (a) Vicinity of ω_1; (b) Vicinity of ω_2. Key: ×, x response amplitude; ×, y response amplitude; ___, threshold for the contact loss.

For instance, Butlin and Woodhouse[23] had observed the onset of hammering phenomenon in their experiment. Meziane et al.[33] experimentally and numerically investigated the squeal phenomenon, and successfully found surface separation dynamics in a beam-on-beam type experiment. In this study, the authors first investigated the linear system through complex eigenvalue solution and obtained a good match between model and experiment in terms of the squeal frequencies. To understand the physical mechanism leading to squeal behavior, a nonlinear transient analysis was then carried out; the effect of contact conditions on squeal initiation was explained both numerically and experimentally. In addition, Aronov et al.[34] experimentally observed a loss of contact within a pin-on-disc setup with an increase in the normal load on the pin. In yet another study by Chen et al.[35], the surface separation between sliding surfaces was related to the major nonlinear interaction leading to the squeal noise. In this study, the results of a nonlinear model are compared to measurements from a bench experiment. In particular, they studied the effect of time delay between the dynamic normal load and resulting friction force on the squeal initiation, and observed that this parameter is a key factor affecting the system stability.

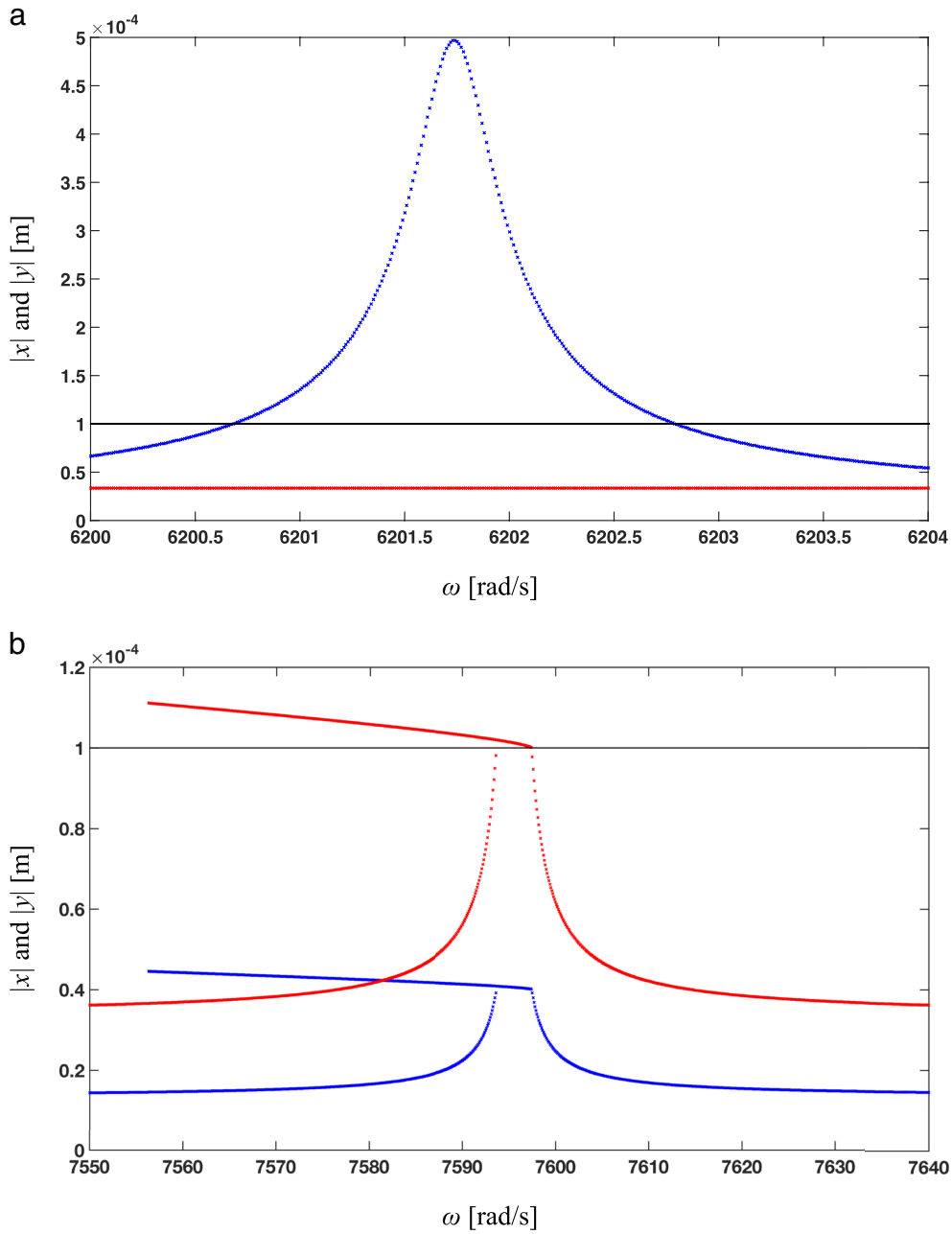

Fig. 11—Nonlinear frequency response of the simplified model (model A4) for $\alpha_1 = \pi$, $\alpha_2 = \pi/2$. (a) Vicinity of ω_1; (b) Vicinity of ω_2. Key: ×, x response amplitude; ×, y response amplitude; ___, threshold for the contact loss.

From the perspective of noise control, both passive and active control approaches have been applied by prior researchers. Application of the passive damping material[36–38] has been employed to suppress squeal noise. In such studies, damping is mostly applied on the brake pad as a constrained layer damping, although the selection of the pad material seems to require rigorous modal tests and brake dynamometer experiments. In terms of the active control, piezoelectric stacks were used as the excitation sources (at ultrasonic frequencies) although the improvements have been limited to particular brake systems at certain frequencies[39–41]. Overall, there is a need for a dedicated bench experiment that could be utilized to validate the model presented here and to seek the noise reduction concepts.

9 CONCLUSION

The chief contribution of this article is the development of a new minimal order mechanical system model that overcomes the limitations of prior work[12–14]. In particular, a two-degree-of-freedom mechanical system is built with kinematic, friction and clearance (in terms of the contact loss) nonlinearities. The nonlinear governing equations

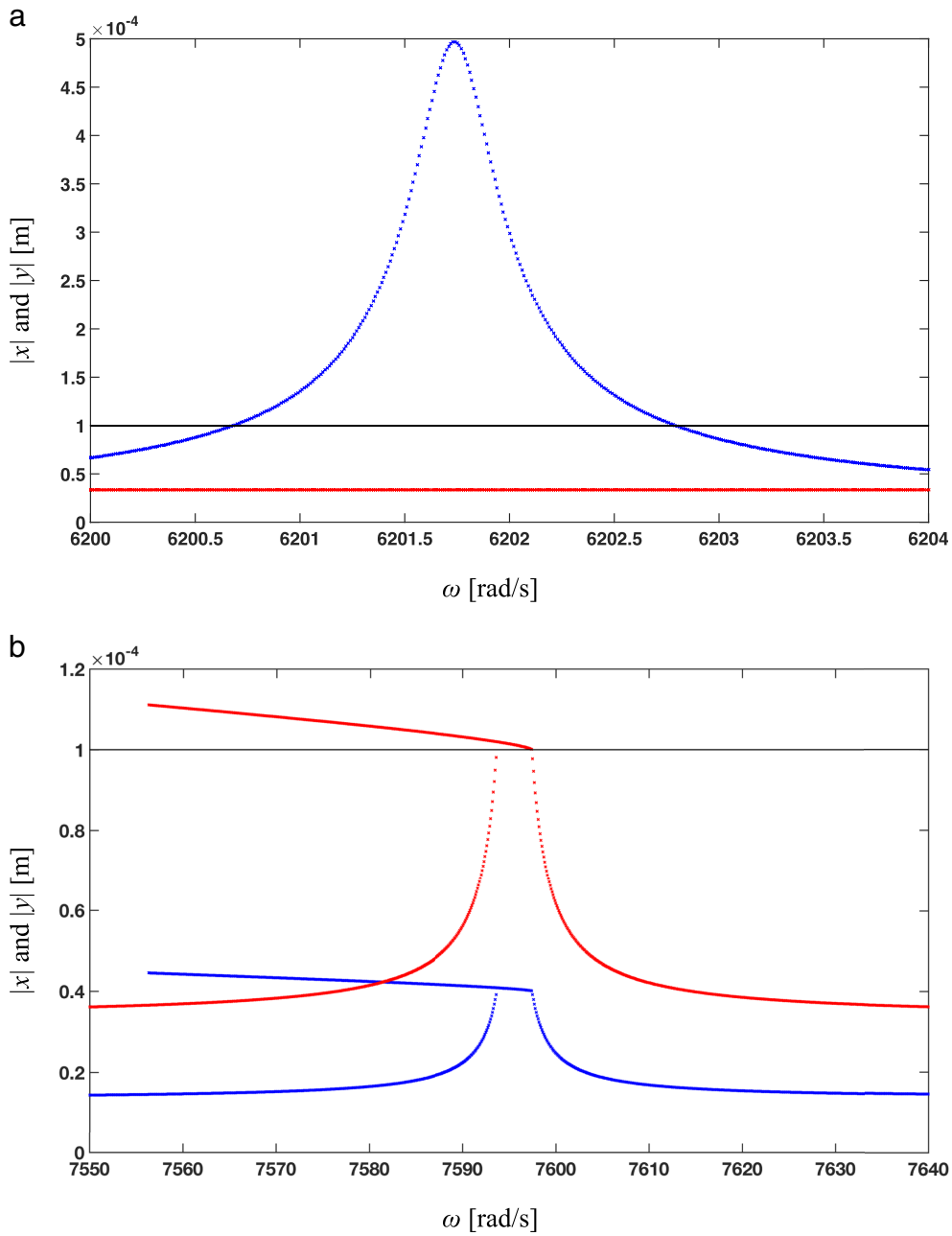

Fig. 12—Nonlinear frequency response of the simplified model (model A4) for $\alpha_1 = \alpha_2 = 3\pi/4$. (a) Vicinity of ω_1; (b) Vicinity of ω_2. Key: ×, x response amplitude; ×, y response amplitude; ___, threshold for the contact loss.

are numerically solved for selected angular arrangements of the inclined springs. Dynamic responses such as perpetual contact, surface separation, unstable motions and limit cycle behavior are successfully obtained, although it is observed that the two-degree-of-freedom model fails to identify the differences between dynamic responses of certain kinematic configurations. The quasi-static sliding motion and dynamic stability maps are obtained with the linearized model. The results reveal that this particular system exhibits unstable dynamics only when the quasi-static sliding motion is not possible. Investigations suggest that stability analysis, based on the linearized system, is not valid over the entire range of spring kinematic arrangements since the assumptions made for the linearization are in conflict with the dynamic responses of corresponding nonlinear system. In support of this claim, the inadequacy of linear system based stability analysis has also been observed by several recent investigators[27–30]. The natural frequencies of the system are investigated for contact and surface separation cases with a simplified model, where all the nonlinearities except the contact loss are ignored. It is seen that the region where the first natural frequency is zero expands when the surfaces are separated. Similarly, the region where the second natural frequency

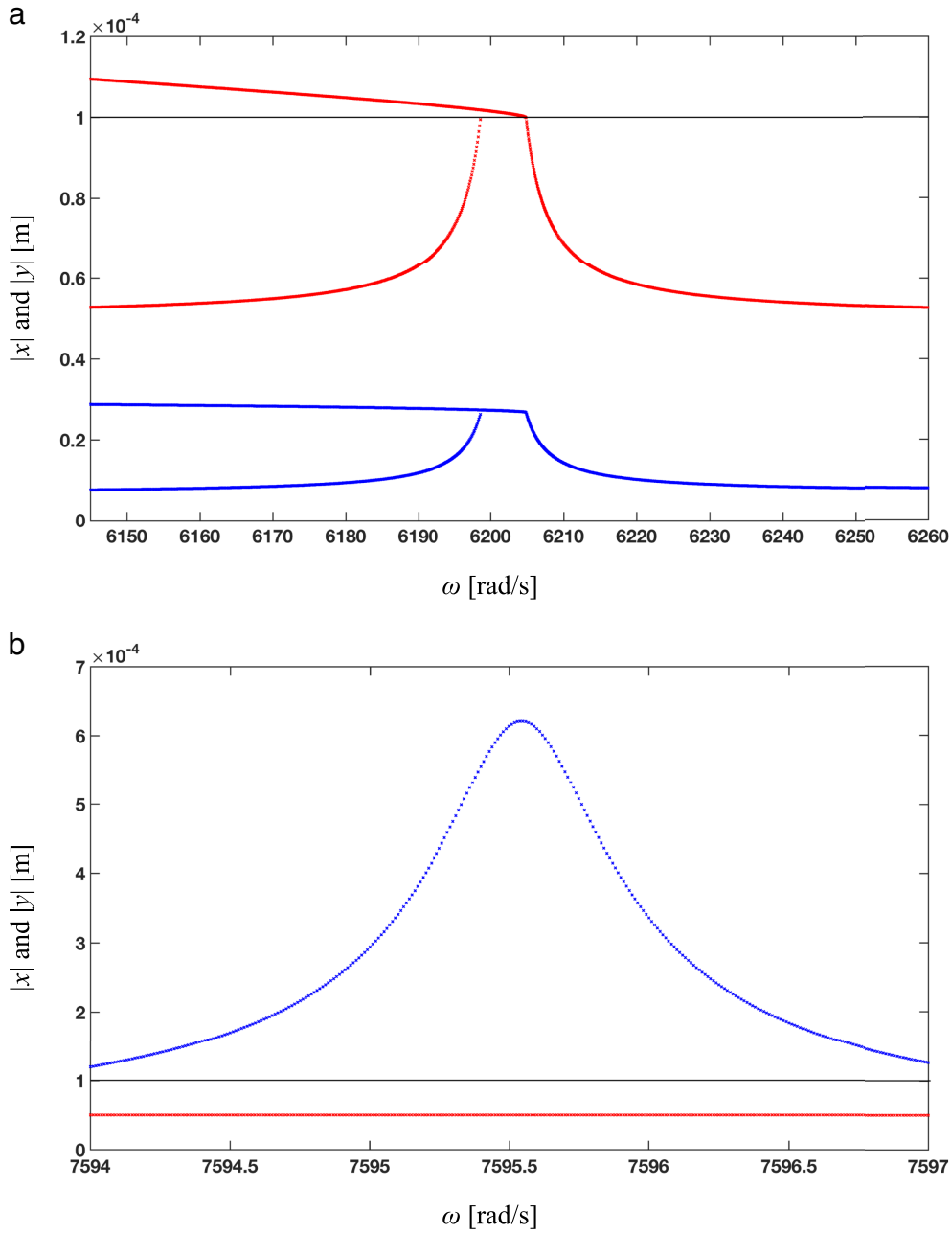

Fig. 13—Nonlinear frequency response of the simplified model (model A4) for $\alpha_1 = \alpha_2 = 5\pi/6$. (a) Vicinity of ω_1; (b) Vicinity of ω_2. Key: ×, x response amplitude; ×, y response amplitude; ___, threshold for the contact loss.

is maximum expands under surface separation case as compared to the full contact case. Finally, nonlinear frequency responses of the simplified model are constructed with the multi-term harmonic balance method. Similar trends are observed in both time and frequency domain solutions. Furthermore, it is seen that the modes of the two-degree-of-freedom model switch when the surface separation occurs as compared to full contact cases.

Of more importance is the observation that the configuration of the brake pad (in terms of its constraints) is a crucial issue, as system stability can be affected by the directions of the normal force vectors that essentially push the brake pad towards the brake disc. Furthermore, it is understood that the contact loss nonlinearity must not be ignored in squeal source models. Nonetheless, this model with only a point contact has certain limitations, and therefore, the development of a more refined minimal order model is desired.

10 NOMENCLATURE

Symbols:

a, **b**, **c**, **d**: Fourier coefficient vectors

$\mathbf{D}$: Differential operator matrix
$\mathbf{h}, \mathbf{g}$: Discontinuous functions in vector form
F: Force
$\mathbf{J}$: Jacobian matrix
k: Spring stiffness
L : Free length of the springs
m: Mass
r: Position vector
R: Reaction force
$\mathbf{R}$: Residue vectors
V: Velocity of the sliding surface
x, y: Spatial coordinates
X, Y: Nondimensional spatial coordinates
α: Angular orientation of springs
μ: Friction coefficient
ω: Natural frequency
σ: Regularizing factor
t: Time coordinate
τ: Nondimensional time coordinate
θ: Independent variable in spatial domain
$\mathbf{\Gamma}$: Discrete Fourier Transform matrix

Subscripts:
f: Fixed end of the spring position vector
n: Denote normal direction
pre: Pretension
r: Denote relative motion
s: Denote restoring force
0: Denotes initial configuration
1, 2, 3: Parameter identifier

Superscripts:
$*$: Denotes the state variables at static equilibrium
T: Transpose operator

11 ACKNOWLEDGMENTS

Support from the Scientific and Technological Research Council of Turkey (3001 Starting R&D Projects Funding Program, Project No: 115 M002) and Scientific Research Projects Coordination Unit at Istanbul Technical University (Project No: MGA-2018-41304) is gratefully acknowledged by the first author. The second author thanks the National Science Foundation's I/UCRC program (www. nsf.gov/eng/iip/iucrc) and the Smart Vehicle Concepts Center (www.SmartVehicleCenter.org) for partially supporting this research.

12 REFERENCES

1. N.M. Kinkaid, O.M. O'Reilly, and P. Papadopoulos, "Automotive disc brake squeal", *J. Sound Vib.*, **267**(1), 105–166, (2003).
2. A. Papinniemi, J.C.S. Lai, J. Zhao, and L. Louder, "Brake squeal: a literature review", *Appl. Acoust.*, **63**(4), 391–400, (2002).
3. S.K. Rhee, P.H.S. Tsang, and Y.S. Wang, "Friction-induced noise and vibration of disc brakes", *Wear*, **133**, 39–45, (1989).
4. F. Chen, S.E. Chen, J. Her, and P. Harwood, "Disc brake intermittent squeal noise study using experimental techniques based systematic approach", *SAE Technical Papers*, 2000-01-0731, (2000).
5. H. Ouyang and J. Mottershead, "Friction induced parametric resonances in discs: effect of a negative friction-velocity relationship", *J. Sound Vib.*, **209**, 251–264, (1998).
6. R.T. Spurr, "A theory of brake squeal", *Proc. Inst. Mech. Eng., Part D*, **1**, 33–52, (1961).
7. M. Nishiwaki, "Generalized theory of brake noise", *Proc. Inst. Mech. Eng., Part D*, **207**, 195–202, (1993).
8. S.S. Chan, J.E. Mottershead, and M.P. Cartmell, "Parametric resonances at subcritical speeds in discs with rotating frictional loads", *Proc. Inst. Mech. Eng., Part C*, **208**, 417–425, (1994).
9. S. Oberst and J.C.S. Lai, "Chaos in brake squeal noise", *J. Sound Vib.*, **330**, 955–975, (2011).
10. U.v. Wagner, D. Hochlenert, and P. Hagedorn, "Minimal models for disk brake squeal", *J. Sound Vib.*, **302**, 527–539, (2007).
11. T. Butlin and J. Woodhouse, "Friction-induced vibration: should low-order models be believed?" *J. Sound Vib.*, **328**, 92–108, (2009).
12. T. Hamabe, I. Yamazaki, K. Yamada, H. Matsui, S. Nakagawa, and M. Kawamura, "Study of a method for reducing drum brake squeal", *SAE Technical Papers*, 1999-01-0144, (1999).
13. N. Hoffmann, M. Fischer, R. Allgaier, and L. Gaul, "A minimal model for studying properties of the mode-coupling type instability in friction induced oscillations", *Mech. Res. Commun.*, **29**, 197–205, (2002).
14. N. Hoffmann and L. Gaul, "Effects of damping on mode-coupling instability in friction induced oscillations", *J. Appl. Math. Mech.*, **83**, 524–534, (2003).
15. S. Kruse, M. Tiedemann, B. Zeumer, P. Reuss, H. Hetzler, and N. Hoffmann, "The influence of joints on friction induced vibration in brake squeal", *J. Sound Vib.*, **340**, 239–252, (2015).
16. S. Oberst and J.C.S. Lai, "Nonlinear friction coupling in disc brake squeal", 18th International Congress on Sound & Vibration, Rio de Janeiro, Brazil, (2011).
17. L. Charroyer, O. Chiello, and J.-J. Sinou, "Parametric study of the mode coupling instability for a simple system with planar or rectilinear friction", *J. Sound Vib.*, **384**, 94–112, (2016).
18. L. Charroyer, O. Chiello, and J.-J. Sinou, "Self-excited vibrations of a non-smooth contact dynamical system with planar friction based on the shooting method", *Int. J. Mech. Sci.*, **144**, 60–101, (2018).
19. N. Hoffmann and L. Gaul, "A sufficient criterion for the onset of sprag-slip oscillations", *Arch. Appl. Mech.*, **73**, 650–660, (2004).
20. V.N. Pilipchuk and C.A. Tan, "Creep-slip capture as a possible source of squeal during decelerated sliding", *Nonlinear Dynam.*, **35**, 259–285, (2004).
21. V. Pilipchuk, P. Olejnik, and J. Awrejcewicz, "Transient friction induced vibrations in a 2-DOF model of brakes", *J. Sound Vib.*, **344**, 297–312, (2015).
22. S. Oberst, J.C.S. Lai, and S. Marburg, "Guidelines for numerical vibration and acoustic analysis of disc brake squeal using simple models of brake systems", *J. Sound Vib.*, **332**, 2284–2299, (2013).
23. T. Butlin and J. Woodhouse, "A systematic experimental study of squeal initiation", *J. Sound Vib.*, **330**, 5077–5095, (2011).
24. O.T. Sen, J.T. Dreyer, and R. Singh, "Order domain analysis of speed-dependent friction induced torque in a brake experiment", *J. Sound Vib.*, **331**, 5040–5053, (2012).
25. O.T. Sen, J.T. Dreyer, and R. Singh, "Envelope and order domain analyses of a nonlinear torsional system decelerating under multiple order frictional torque", *Mech. Syst. Signal Process.*, **35**, 324–344, (2013).
26. T.C. Kim, T.E. Rook, and R. Singh, "Effect of smoothening functions on the frequency response of an oscillator with clearance nonlinearity", *J. Sound Vib.*, **263**, 665–678, (2003).
27. D. Hochlenert, "Nonlinear stability analysis of a disc brake model", *Nonlinear Dynam.*, **58**, 63–73, (2009).
28. J.J. Sinou, "Transient non-linear dynamic analysis of automotive disc brake squeal — on the need to consider both stability and nonlinear analysis", *Mech. Res. Commun.*, **37**, 96–105, (2010).

29. K. Soobbarayen, J.J. Sinou, and S. Besset, "Numerical study of friction-induced instability and acoustic radiation — effect of ramp loading on the squeal propensity for a simplified brake model", *J. Sound Vib.*, **333**, 5475–5493, (2014).
30. Z. Zhang, S. Oberst, and J.C.S. Lai, "On the potential of uncertainty analysis for prediction of brake squeal propensity", *J. Sound Vib.*, **377**, 123–132, (2016).
31. S. Oberst and J.C.S. Lai, "Pad-mode-induced instantaneous mode instability for simple models of brake systems", *Mech. Syst. Signal Process.*, **62-63**, 490–505, (2015).
32. S. Oberst and J.C.S. Lai, "Nonlinear transient and chaotic interactions in disc brake squeal", *J. Sound Vib.*, **342**, 272–289, (2015).
33. A. Meziane, L. Baillet, and B. Laulagnet, "Experimental and numerical investigation of friction induced vibration of a beam-on-beam in contact with friction", *Appl. Acoust.*, **71**, 843–853, (2010).
34. V. Aronov, A.F. D'Souza, S. Kalpakjian, and I. Shareef, "Interactions among friction, wear, and system stiffness—part 1: effect of normal load and system stiffness", *J. Tribol.*, **106**, 54–59, (1984).
35. G.X. Chen, Q.Y. Liu, X.S. Jin, and Z.R. Zhou, "Stability analysis of a squealing vibration model with time delay", *J. Sound Vib.*, **311**, 516–536, (2008).
36. M. Triches, S.N.Y. Gerges, and R. Jordan, "Reduction of squeal noise from disc brake systems using constrained layer damping", *J. Braz. Soc. Mech. Sci. Eng.*, **26**, 340–348, (2004).
37. K.B. Dunlap, M.A. Riehle, and R.E. Longhouse, "An investigative overview of automotive disc brake noise", *SAE Technical Papers*, 1999-01-0142, (1999).
38. H. Festjens, C. Gael, R. Franck, D. Jean-Luc, and L. Remy, "Effectiveness of multilayer viscoelastic insulators to prevent occurences of brake squeal: a numerical study", *Appl. Acoust.*, **73**, 1121–1128, (2012).
39. K.A. Cunefare and A.J. Graf, "Experimental active control of automotive disc brake rotor squeal using dither", *J. Sound Vib.*, **250**, 579–590, (2002).
40. Y. Nishizawa, H. Saka, S. Nakajima, and T. Arakawa, "Electronic control cancelling system for a disc brake noise", *SAE Technical Papers*, 971037, (1997).
41. C.Y. Teoh and Z. MohdRipin, "Dither effect on drum brake squeal", *J. Vib. Control.*, **23**, 1057–1072, (2017).